Conf-930222--57

UCRL-JC-112603
PREPRINT

Dynamic Thermal Tomography for Nondestructive Inspection of Aging Aircraft

N. K. Del Grande, K. W. Dolan, P. F. Durbin
M. R. Gorvad and A. B. Shapiro

This paper was prepared for submittal to the
SPIE International Symposium on Optical Applied Science
San Diego, California
July 11-16, 1993

November 1993

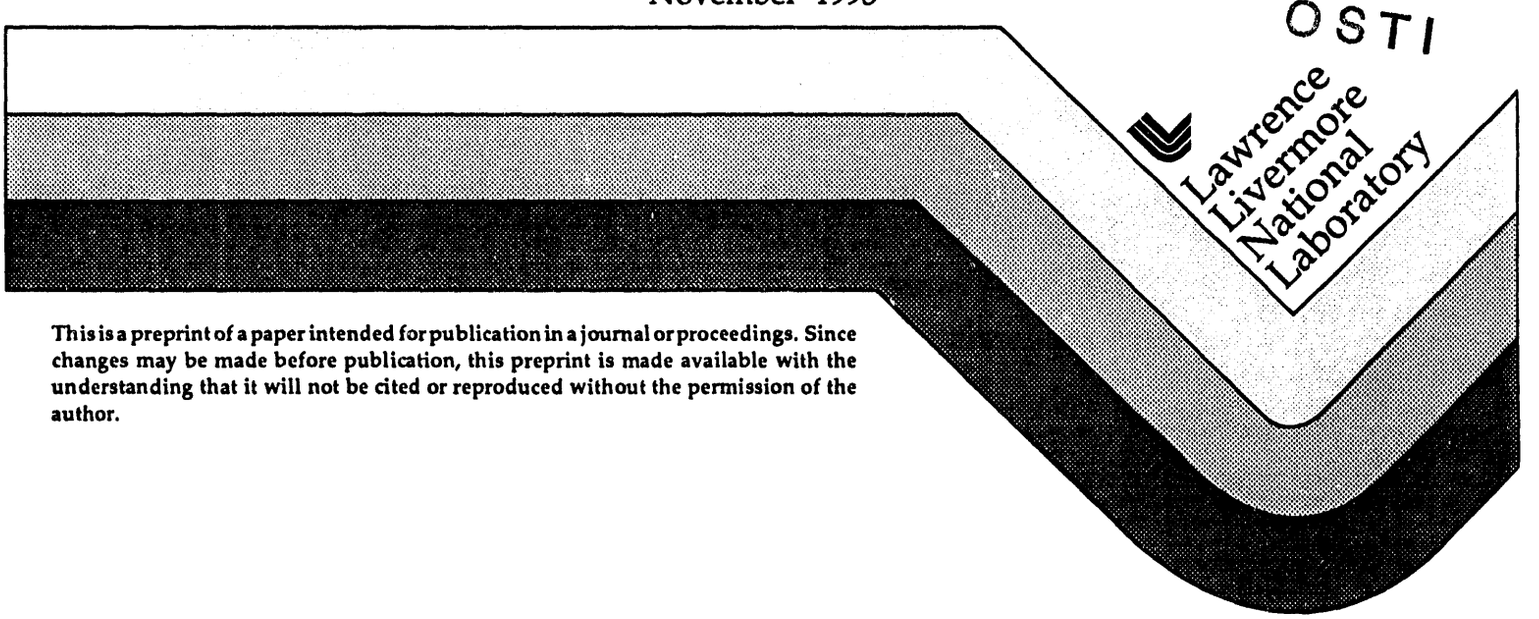

DISCLAIMER

Dynamic thermal tomography for nondestructive inspection of aging aircraft

N. K. Del Grande, K. W. Dolan, P. F. Durbin, M. R. Gorvad and A. B. Shapiro

Lawrence Livermore National Laboratory
P. O. Box 808, Livermore CA 94550

ABSTRACT

We apply dual-band infrared (DBIR) imaging as a dynamic thermal tomography tool for wide area inspection of a Boeing 737 aircraft (owned by the FAA/AANC at the Sandia hangar in Albuquerque, NM) and several Boeing KC-135 aircraft panels (used for the round robin experiment conducted at Tinker AFB, OK). Our analyses are discussed in this report. After flash-heating the aircraft skin, we record synchronized DBIR images every 40 ms, from onset to 8 seconds after the heat flash. We analyze selective DBIR image ratios which enhance surface temperature contrast and remove surface-emissivity clutter (from dirt, dents, tape, markings, ink, sealants, uneven paint, paint stripper, exposed metal and roughness variations). The Boeing 737 and KC-135 aircraft fuselage panels have varying percent thickness losses from corrosion. We established the correlation of percent thickness loss with surface temperature rise (above ambient) for a partially corroded F-18 wing box structure (with a 2.9 mm uncorroded thickness) and several aluminum plates (with 1.0, 1.1, 2.3 and 3.9 mm thicknesses) which had 6 to 60 % thickness losses at milled flat-bottom hole sites. Based on this correlation, lap splice temperatures rise 1 °C per 24 ± 5 % material loss at 0.4 s after the heat flash. We tabulate and map corrosion-related percent thickness loss effects (related to the corresponding surface temperature rise at 0.4 s after the heat flash) for the riveted (and bonded) Boeing 737, and the riveted (but unbonded) Boeing KC-135. We map the fuselage composite thermal inertia, $(k\rho c)^{1/2}$, based on the (inverse) slope of the surface temperature versus inverse square root of time. Composite thermal inertia maps characterize shallow skin defects within the lap splice at early times (<0.3 s) and deeper skin defects within the lap splice at late times (>0.4 s). Late time composite thermal inertia maps depict where corrosion-related thickness losses occur (e.g., on the inside of the Boeing 737 lap splice, beneath the galley and the latrine). Lap splice sites on a typical Boeing KC-135 panel with low composite thermal inertia values had high skin-thickness losses from corrosion.

1.0 INTRODUCTION

Dual-band infrared (DBIR) imaging was pioneered by LLNL as a precise temperature survey technique to depict small temperature differences resulting from heat flow anomalies. Previous successful applications of DBIR imaging (from aircraft, helicopter, tower and raised platforms) detected underground and obscured object sites with 0.2 °C or more surface temperature differences from:

- geothermal aquifers under 6 to 60 meters of dry soil [1,2]
- cemetery walls, trenches and a building foundation under 80 cm of asphalt and debris [3]
- buried mines, rocks and objects under 1 to 20 cm of disturbed sand, soil, or sod [3-8]
- sea ice thicknesses varying from 5 to 50 cm. [9,10]

This paper discusses the analysis of DBIR images to identify hidden defects within flash-heated test specimens and aircraft structures. We are developing a wide-area, non-contact, non-destructive inspection (NDI) tool to depict hidden defects within:

- adhesively-bonded aluminum lap joints with disbond (no-adhesive) sites replicating the skin of a Boeing 737 aircraft [9,11,12]
- a Boeing 737 aircraft owned by the FAA/AANC NDI Validation Center at the Sandia hangar in Albuquerque, NM
- calibration plates with milled flat-bottom holes replicating material losses for a corroded Boeing KC-135 aircraft lap splice
- a F-18 wing box structure from Northrop Corporation with measured material losses and by-products of corrosion
- several Boeing KC-135 aircraft panels dismantled after the round robin NDI experiments conducted at Tinker AFB, OK

Using judiciously selected DBIR image ratios (from cameras which record the infrared at 3-5 μm and 8-12 μm) we enhance surface temperature contrast and remove the mask of surface emissivity clutter. By removing the clutter mask (from dirt, dents, tape, markings, ink, sealants, uneven paint, paint stripper, exposed metal and roughness variations) we clarify interpretation of surface temperature anomalies associated with hidden defect sites. The basis for this is described in the following section.

2.0 POWER LAW MODEL

A power law model [13] explains how infrared signals vary as a function of the surface emissivity and the surface's absolute temperature:

$$I_\lambda \sim e_\lambda T^{50/\lambda} \quad , \tag{1}$$

where I_λ is the intensity at a given wavelength, e_λ is emissivity at that wavelength, T is in temperature in Kelvin and λ is the wavelength in micrometers.

We can obtain temperature alone by computing the ratio

$$R = \frac{I_5}{I_{10}} = \frac{e_5 T^{50/5}}{e_{10} T^{50/10}} = \frac{e_5}{e_{10}} T^5 \quad , \tag{2}$$

For a greybody, $e_5 = e_{10}$ and $R \sim T^5$.

We can obtain the emissivity ratio by computing

$$\frac{(I_{10})^2}{I_5} = \frac{(e_{10})^2 (T^5)^2}{e_5 T^{10}} = \frac{(e_{10})^2}{e_5} \tag{3}$$

This ratio is sensitive mostly to surface objects which have very different emissivities at 5 and 10 micrometers (most metal surfaces). We then compute the DBIR ratios to obtain enhanced temperature contrast (T^5) and emissivity-ratio (E-ratio) maps:

$$(T/T_{av})^5 = (S/S_{av}) / (L/L_{av}) \quad \text{and} \quad \text{E-ratio} = (L/L_{av})^2 / (S/S_{av}) \tag{4}$$

where S is the short-wavelength intensity (e.g., I_5), S_{av} is the average value of the pixels in S, L is the long wavelength intensity (e.g., I_{10}) and L_{av} is the average value of the pixels in L. See Figure 1 for the Boeing 737 application of (EQ 4).

3.0 THERMAL RESPONSE TO HEAT FLASH

To describe the results of our aircraft measurements, we refer to the heat diffusion equation, which is:

$$\rho c \frac{\partial T}{\partial t} = k \nabla^2 T \tag{5}$$

The solution of (EQ 5) for a semi-infinite solid with an instantaneous surface heat flux is: [14]

$$T(x,t) = \frac{q}{\sqrt{4\pi k \rho c t}} \exp\left(-\frac{x^2}{4\alpha t}\right) \tag{6}$$

where T is temperature, x is the distance from surface, k is thermal conductivity, ρ is density, c is heat capacity, α is thermal diffusivity, t is time and q is the surface heat flux. For a semi-infinite solid approximation, the surface temperature is proportional to the inverse square root of time. This describes our measured results in Figure 2 for an aluminum plate with flat-bottom holes, Figures 3 and 5, the Boeing 737 aircraft fuselage, and Figures 4 and 6, the Boeing KC-135 aircraft panels with measured total lap splice thicknesses (including the lap, doubler, stringer and patch) varying from 4.2 to 7.5 mm. Whereas Figures 2-6 give examples of temperature-time responses in agreement with (EQ 6), the solution of (EQ 6) at several depths as a function of time is shown graphically in Figure 7. Our analyses focus on the effects of corrosion within aircraft lap splice structures backed by a combination of doublers, tear straps, stringers or patches (not visible from the front surface).

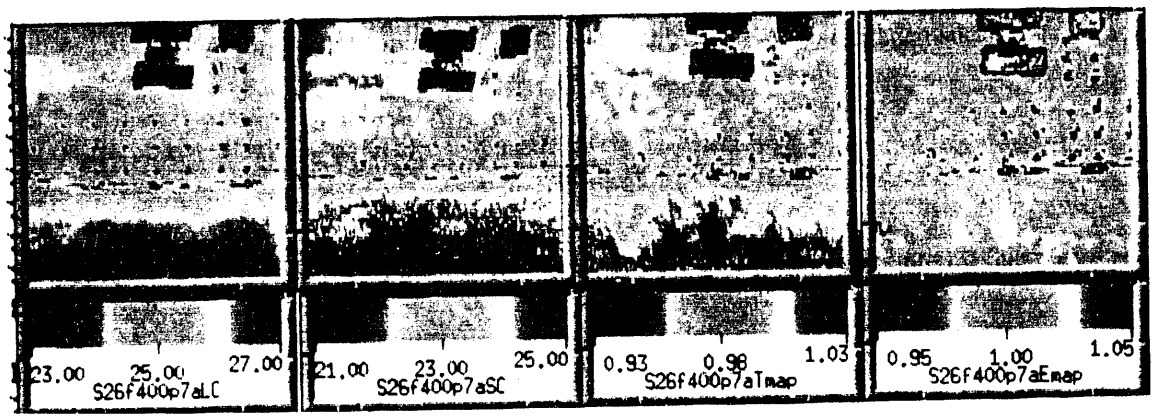

Figure 1. Maps (left to right) of Boeing 737 lap splice structure with hidden defects showing 10 μm and 5 μm apparent temperatures (°C), dual-band infrared (DBIR) enhanced temperatures (relative scale) and emissivity differences from clutter.

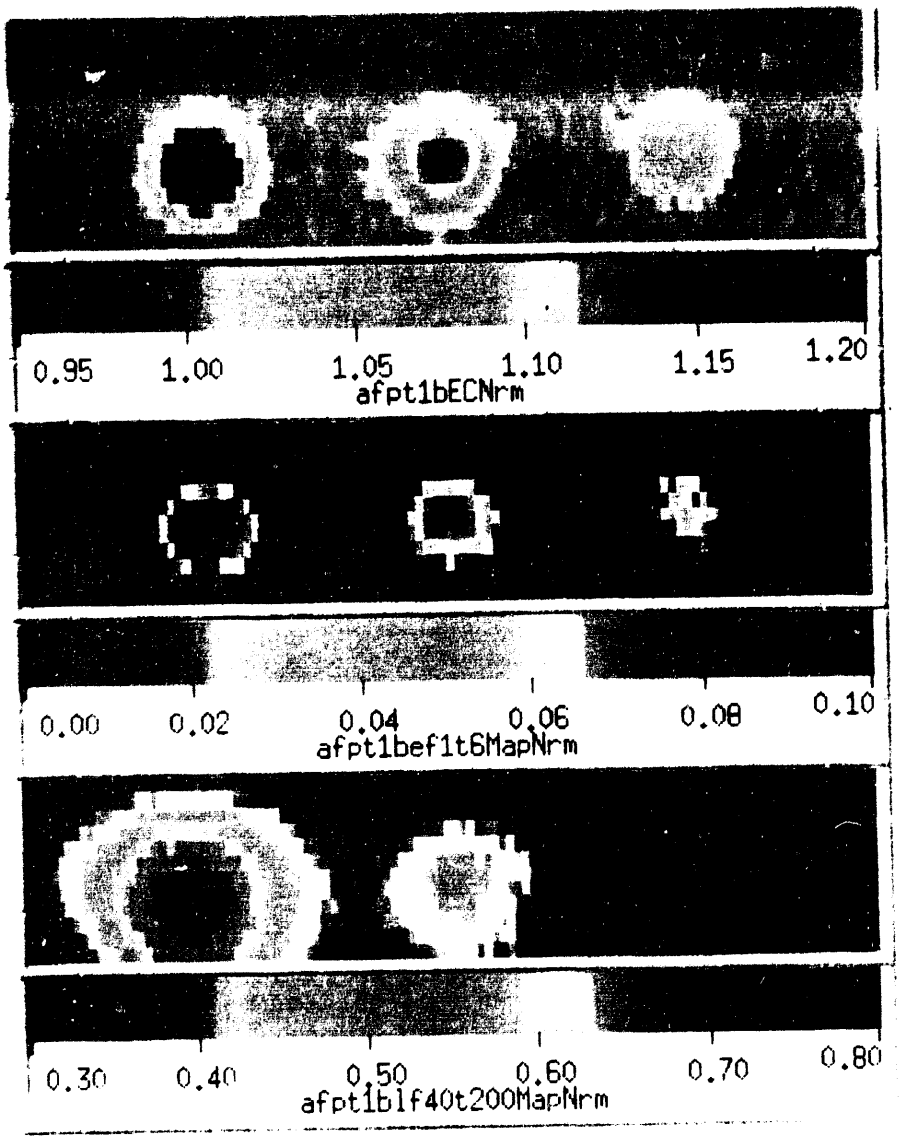

Figure 2. Top: relative temperature response 40 ms after heat flash; center and bottom: thermal inertia at early times (0.0 to 0.2 s) and late times (1.6 to 8.0 s) for 63%, 42% and 21% (left to right) flat-bottom holes in 0.95 mm aluminum plate.

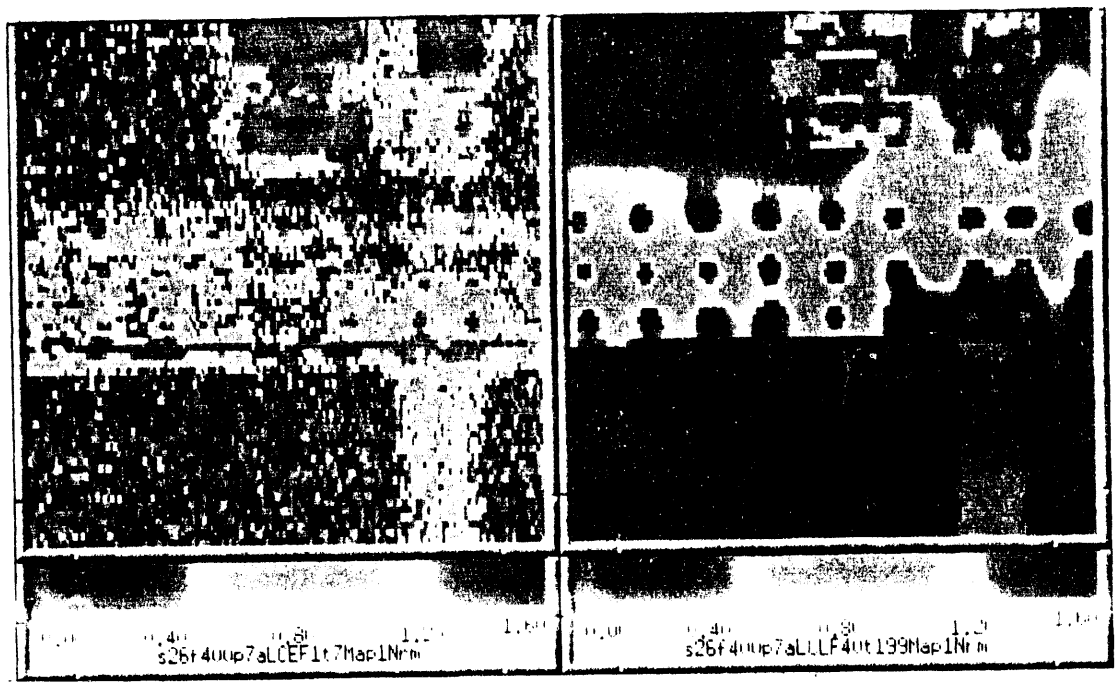

Figure 3. Boeing 737 relative thermal inertia maps, showing at left: early-time (0.0 to 0.3 s) and at right: late-time (1.6 to 8.0 s) defect sites within the (~1mm) aluminum skin (adhesively-bonded) lap splice. Note late-time thermal inertia lows (green butterfly-like pattern) where corrosion may have entered the inside of the lap splice beneath the galley and the latrine.

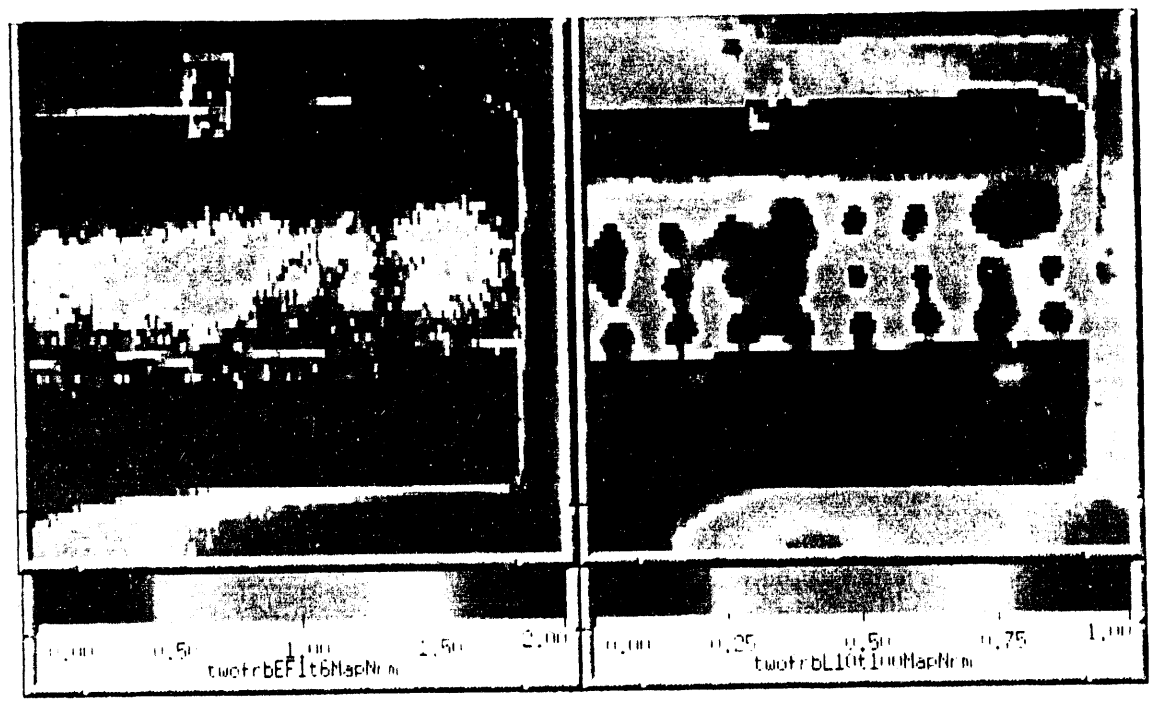

Figure 4. Boeing KC-135 relative thermal inertia maps, showing at left: early-time ((0.0 to 0.2 s) and at right: late-time (0.4 to 4.0 s) defect sites within the (~2 mm) aluminum skin lap splice from material losses and by-products of corrosion. Red areas (with less material loss from corrosion) have bulk thermal properties more resistive to temperature change at late times.

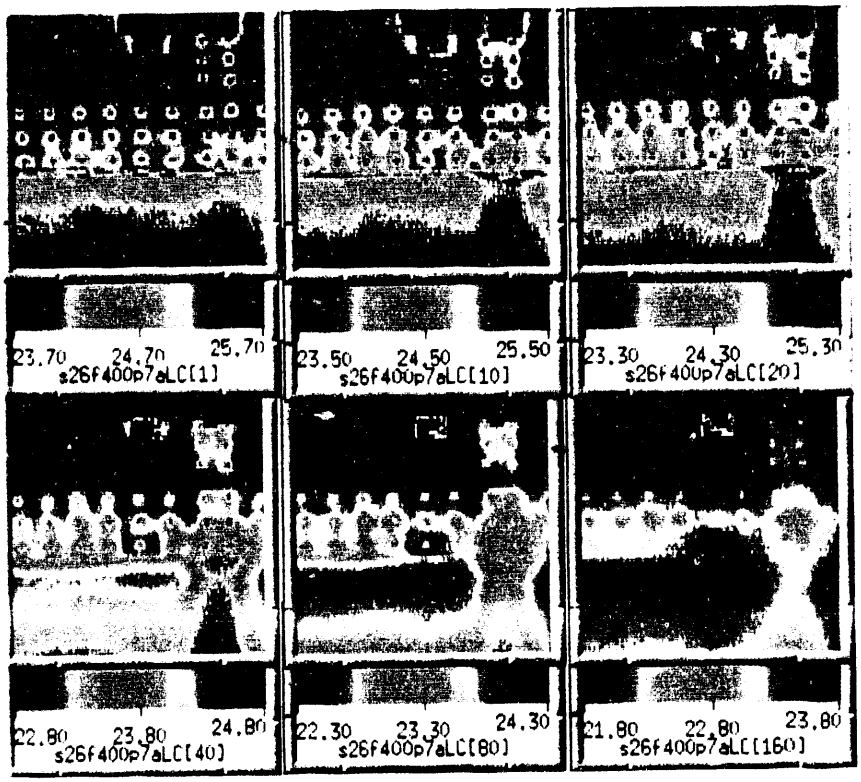

Figure 5. Boeing 737 aircraft lap splice surface temperatures imaged after heat flash. Top (left to right) at 0.04, 0.40 and 0.80 seconds. Bottom (left to right) at 1.6, 3.2 and 6.4 seconds.

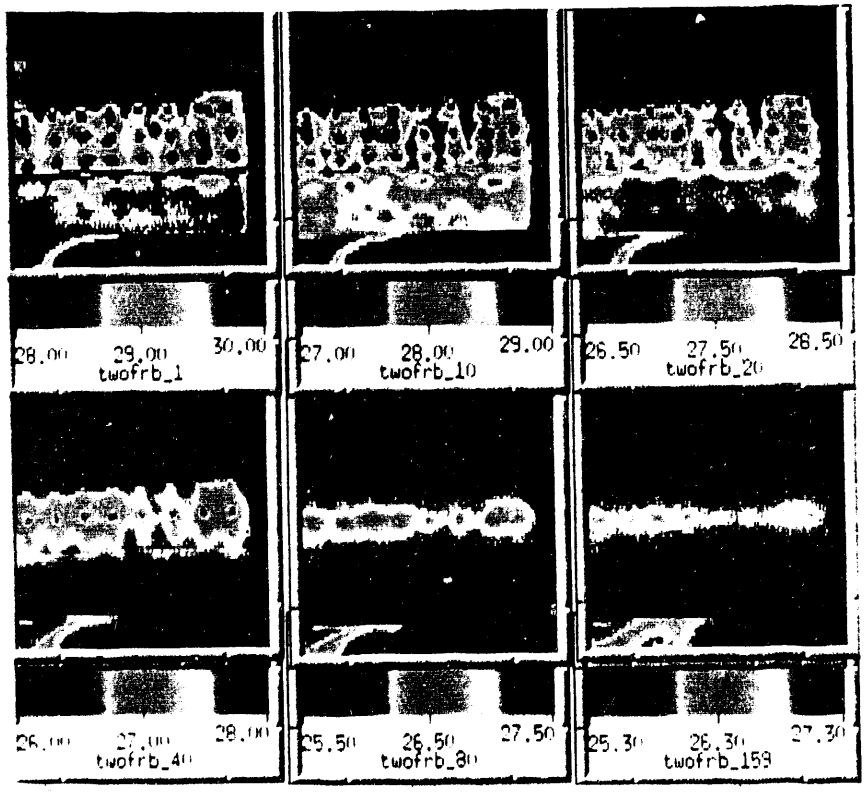

Figure 6. Boeing KC-135 aircraft lap splice surface temperatures imaged after heat flash. Top (left to right) at 0.04, 0.40 and 0.80 seconds. Bottom (left to right) at 1.6, 3.2 and 6.4 seconds.

There are two steps in solving the problem of heat transfer for thinner aircraft skins, apart from the lap splice structures considered in this report. First, during flash lamp heating, the solution to (EQ 5) for an insulated surface at x=0 and flux F applied to the surface at x=l is [14]

$$T = \frac{Ft}{\rho c l} + \frac{Fl}{k}\left\{\frac{3x^2 - l^2}{6l^2} - \frac{2}{\pi^2}\sum_{n=1}^{\infty}\frac{(-1)^n}{n^2}\exp\left(\frac{-\alpha n^2\pi^2 t}{l^2}\right)\cos\left(\frac{n\pi x}{l}\right)\right\} \tag{7}$$

Secondly, there is heat redistribution in the slab. The solution of (EQ 5) when the slab has an initial temperature distribution of f(x), calculated from (EQ 7) at the end of the flash lamp heating, and with both surfaces insulated is [14]

$$T = \frac{1}{l}\int_0^l f(x)dx + \frac{2}{l}\sum_{n=1}^{\infty}\exp\left(\frac{-\alpha n^2\pi^2 t}{l^2}\right)\cos\left(\frac{n\pi x}{l}\right)\int_0^l f(x)\cos\left(\frac{n\pi x}{l}\right)dx \tag{8}$$

Heat loss by convection has been omitted. This is justified over the short time scale of this problem because the thermal conduction conductance (conductance due to heat loss by conduction) is 240,000 W/m^{2}sec, while the conductance due to heat loss by convection is only 5 W/m^{2}sec. Testing the validity of these analytical solutions and reporting our results is beyond the scope of this paper. Apart from the thicker lap splice areas, covered in this paper, there are other areas with thinner (1.0 mm and 1.5 mm single thickness) aircraft skins.

This problem was modeled using TOPAZ-2D.[15] Parameters chosen were:

- heat lamp surface flux F=1.5 10^6 W/m^2 for 0.004 sec
- slab thickness l=0.001 m
- aluminum ρ=2700 Kg/m^3, k=240 W/m sec, c=920 J/KgC
- aluminum oxide ρ=1200 Kg/m^3, k=25 W/m sec, c=780 J/KgC

Temperature histories at several depth locations [(a) x=0, (b) x=0.25 mm, (c) x=0.50 mm, (d) x=0.75 mm, (e) x=1.00 mm] are shown in figures 8 and 9. Figure 8 is the time response for a 1.00 mm thick aluminum slab. Figure 9 is the time response for a composite slab consisting of aluminum (0.9 mm) with a corrosion layer (0.1 mm) of aluminum oxide.

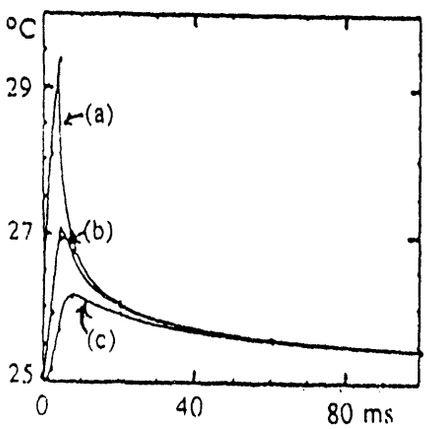

Figure 7. The temperature-time response of (Eq. 6) for a semi-infinite aluminum slab at the surface (a) and at depths of 0.50 mm (b) and 1.0 mm (c).

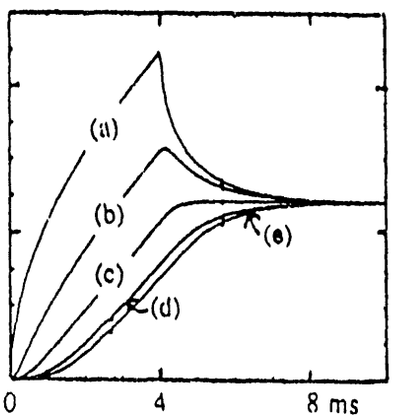

Figure 8. The temperature-time response for a 1 mm thick aluminum slab at depths of x = 0 mm (a), x = 0.25 mm (b), x = 0.50 mm (c), x = 0.75 mm (d), x = 1.0 mm (e).

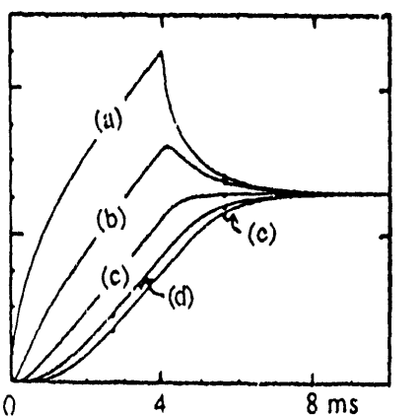

Figure 9. The temperature-time response for a 1 mm thick slab of aluminum (0.9 mm) and aluminum oxide (0.1 mm) at depths of x = 0 mm (a), x = 0.25 mm (b), x = 0.50 mm (c), x = 0.75 mm (d), x = 1.0 mm (e).

4.0 EXPERIMENTAL EQUIPMENT, SETUP AND TEST PROCEDURE

4.1 Experimental equipment

The following equipment was used for the demonstration of DBIR imaging as a dynamic thermal tomography tool for nondestructive inspection (NDI) of the FAA Boeing 737 aircraft at the Sandia National Laboratory hangar in Albuquerque, NM. Similar equipment was used to inspect the Boeing KC-135 panels, which were dismounted from the Tinker AFB aircraft in Oklahoma and transported to the Lawrence Livermore National Laboratory in Livermore, CA.

- Infrared scanner - Agema 880 dual band Burst Recording Unit (BRU) with the 3-5 micron and 8-12 micron DBIR scanners, a 12 bit digital image processor and a 1.3 G-Byte hard drive.
- Color printer - Mitsubishi CP210.
- Flash lamps - 3 Norman 4000 Joule and 1 Balcor 6000 Joule lamps, LLNL flash lamp control box, and LLNL adjustable flash lamp/scanner positioning stand.
- Image processing workstation - Silicon Graphics Indigo R-3000 with 2 - 1.2 G-Byte hard drives and 48 M-Bytes of memory.
- Visual images - 35 mm (still) and 8 mm (video) cameras.

4.2 Experimental setup

For effective nondestructive inspection of highly reflective (unpainted) aluminum panels, we prepare the target surface to increase the thermal gain from the flash lamps. This gain increase provides the temperature contrast needed to resolve subtle differences which distinguish hidden defects within aircraft lap splice structures from background noise. To this end, we spray paint the area of interest on the aircraft skin using Crayola black (water removable) paint. Portable (welding) shields isolate the flash lamps from the operator or other personnel in the area, thereby providing a safe working environment.

The dual-band (Agema 880) infrared scanners are mounted on a positioning stand and co-aligned to image the same field of view at a distance of 26 inches from the test panel. Four flash lamps are positioned 16 inches from the panel and angled to provide uniform heating. The flash lamps are arranged in a square array (24 inches on a side). They are connected to the flash lamp control box and to the Agema computer. The operator presses a firing button. This triggers the flash lamps and synchronizes the timing to start a data capture sequence 2.8 ms after the lamps fire. A typical sequence is 50 frames. Each frame has a duration of 160 ms. A frame consists of 4 interlaced fields, each with a duration of 40 ms. Thus we view on a display screen, record, and subsequently store on the hard drive, 200 consecutive (40 ms duration) DBIR images during the 8 seconds following a 4.2 ms heat flash.

The recently modified FAA/LLNL prototype DBIR system (by Bales Scientific Inc.) includes a continuous line scan capability to time-resolve thermal images from 0 to 400 ms after onset of the flash, in intervals of 550 μs. This will be used to test the predictability of TOPAZ-2D surface temperature calculations (see Figures 8 and 9).

4.3 Experimental procedure

The scanners and lamps are set up as described above. A typical field of view is 28 cm (11 inches). Video camcorders are used to document all areas of interest, whereas 35 mm cameras provide still photographs for special areas of interest. The computer data files are named using the aircraft stringer and frame position numbers. A written log is kept of file names and setup parameters. Small reference squares are taped to the aircraft skin to mark the top center of each IR image. Lap splice sites along the aircraft stringers under inspection are flash heated. The 50 frame (200 field) sequences are recorded at a data capture rate of 25 fields per second. The recorded digital data are verified, the set up is repositioned and the sequence is repeated.

The data on the hard disk is backed up on 1/4 inch streamer tape, transferred to the Silicon Graphics workstation via an ether net connection and backed up on tape from the work station. Initial data analyses were conducted with the Agema software which provided color-coded temperature maps as output from the color printer. Specialized LLNL software codes (which run on the SGI work station) provide enhanced temperature contrast maps, emissivity-ratio maps, thermal inertia maps, dynamic thermal response curves and additional information.

5.0 DBIR IMAGING RESULTS FOR THE BOEING 737 AND KC-135 AIRCRAFT PANELS

5.1 Surface clutter sites distinguished from hidden defect sites

To clarify interpretation, we distinguish between heat transfer anomalies at potential sites which identify hidden aircraft defects and surface (or near surface) clutter. To this end, we use DBIR image ratios to produce enhanced temperature contrast and emissivity-ratio maps. Figure 1 shows (left to right) two apparent temperature maps (recorded at 10 μm and at 5 μm), an enhanced temperature-contrast map, which varies as T^5, and an emissivity-ratio map based on (EQ 2), (EQ 3) and (EQ 4) for the FAA Boeing 737 aircraft (Stringer 26) lap splice.

We note temperature and emissivity-ratio differences for various black cloth (red, hot) and metal (purple, cold) tape markers at the top, right of center, and the masking tape marker (painted black) at the top right corner. Also, we note from the emissivity-ratio map where the black paint was not evenly applied (e.g., beneath the lap splice). The most common types of skin clutter, identified with DBIR image ratios, include: dirt, dents, tape, markings, ink, sealants, uneven paint, paint stripper, exposed metal and roughness variations. We remove clutter sites to correctly identify hidden defect sites.

5.2 Interpretation of dynamic temperature variations for Boeing aircraft panels[16]

Temperature variations with time (after the heat flash) are compared for the Boeing 737 Stringer 26, Station 400 (s26f400.7) in Figure 5 and the Boeing KC-135 Panel 2 (2FR, at the right edge of the 30 inch panel) in Figure 6. We note the 2 °C range at 0.04 s, 0.40 s, 0.80 s (top row, left to right) and at 1.60 s, 3.20 s and 6.40 s (bottom row, left to right), emphasizes dynamic thermal contrast differences between the Boeing 737 and the Boeing KC-135 at (warm, red) lap joint defect sites.

Corrosion within the Boeing 737 (epoxy-bonded) lap splice causes disbonding. Disbonding allows air to be trapped. Trapped air acts like an insulator. It does not allow heat to transfer longitudinally (perpendicular to the front face) by conduction from the front to the back surface as readily as it would without trapped air. This effect is shown in Figure 5 by the near-constant temperature contrast from 0.4 to 3.2 s which is based on our measurements of the FAA/AANC owned Boeing 737. At late times, after 0.4 seconds, the (unbonded) Boeing KC-135 lap splice has a different temperature versus time response (see Figure 6) than the (bonded) Boeing 737 lap splice because it does not have adhesive bonding to mask the correlation between the percentage material loss and the corresponding surface temperature rise associated with corrosion.

Corrosion-related material loss effects are best measured at 0.4 seconds after the heat flash (both for bonded and unbonded lap joints). Temperatures at 0.4 s are sensitive to material loss effects within a lap joint and insensitive to clutter and timing uncertainties (synchronizing the flash lamp with the images recorded at two IR bands). It is early enough to provide a good temperature contrast for sites with and without material loss from corrosion. The 0.4 s measurements are effective regardless of trapped air. At later times, trapped air masks the temperature-time history, characterizing material-loss effects differently for disbonded corrosion sites (surrounded by bonded sites) than for unbonded corrosion sites (surrounded by unbonded sites).

6.0 INTERPRETATION OF TEMPERATURE AND THERMAL INERTIA MAPS

6.1 Aluminum plate with flat-bottom holes

Figure 2 (left to right, top row) shows the color-coded relative temperature response at 40 ms after the heat flash for an aluminum plate (1 mm thick) with 20%, 40% and 62% thickness loss, relative to surroundings, for milled flat-bottom holes. Early-time (less than 0.3 s, middle row) and late-time (more than 0.4 s, bottom row) composite thermal inertia maps in Figure 2 are based on the (inverse) slope of the temperature versus inverse square root of time responses. Heavily corroded lap splice sites with the most material loss are red (hot) in Figures 5 and 6 but green in Figures 3 and 4 since they have low composite thermal inertia and change temperature more readily than their thicker (uncorroded) surroundings.

6.2 Boeing 737 and KC-135 aircraft panels: thermal inertia maps[17,18,19]

Based on empirical data, the slope of the temperature versus inverse square root of time for image data is constant at early times (0.1 s to 0.3 s) as well as late times (2 s to 5 s). The inverse thermal inertia (or effusivity) slope $(k\rho c)^{-1/2}$ (see EQ 6) for a semi-infinite slab, fits the temperature response of the image data particularly well at late times. Based on our calculations, the late time heat transfer is lateral (parallel to the front face of the aircraft skin). Late times thermal inertia effects are sensitive to the deeper fuselage structures (stringers) on the back side of the lap splice. The Boeing KC-135 panels lap splice thicknesses ranged from 4.2 mm to 7.6 mm, which justifies our use of the semi-infinite slab approximation.

In Figure 3, seven early-time (less than 0.28 s, on the left) and 159 late-time (1.6 s to 8.0 s, on the right) images were used to produce composite thermal inertia maps of the Boeing 737 aircraft fuselage, Stringer 26 (s26f400.7) shown above. Note the green "butterfly-like" site on the late-time thermal inertia map where corrosion entered the lap splice from inside the aircraft. This site was beneath the galley and the latrine. Note the relatively low thermal inertia for front-surface cloth and masking tape markers and back surface tear straps (bottom right corner).

In Figure 4, six early-time (less than 0.24 s, on the left) and 90 late-time (0.40 s to 4.0 s, on the right) images were used to produce composite thermal inertia maps of Panel 2 (2FR, at the right edge) shown above. Low thermal inertia sites (with the most material loss from corrosion and the least resistance to temperature change) appear green, whereas high thermal inertia sites (with the smallest percentage of material loss from corrosion and the most resistance to temperature change) appear red.

6.3 Interpretation of Boeing 737 and KC-135 temperature maps and their differences

Examples of temperature variations with time (after the heat flash) are shown in Figure 5 for the Boeing 737 Stringer 26, Station 400 (s26f400.7) and in Figure 6 for the Boeing KC-135 Panel 2 (2FR, at the right edge of the 30 inch panel). For a common (relative) two degrees Celsius range at 0.04 s, 0.40 s, 0.80 s (top left to right) and at 1.60 s, 3.20 s and 6.40 s (bottom left to right), we note the temperature versus time behavior is different for the Boeing 737 and the Boeing KC-135.

In Figure 5, the dynamic temperature (^{o}C) variations for the Boeing 737 aircraft fuselage, Stringer 26, Station 400, centered 0.7 of the way toward the next larger station (s26f400.7) at 0.04 s, 0.40 s, 0.80 s (top left to right) and at 1.60 s, 3.20 s and 6.40 s (bottom left to right) are based on the 10 μm apparent temperature maps. Note minimal change in lap splice above-ambient temperature contrast at (corrosion-related) disbond site (beneath blue, cold, tape marker) from 0.4 s to 3.2 s.

In Figure 6, the dynamic temperature variations for the Boeing KC-135 Panel 2 (2FR, at the right edge) at 0.04 ms, 0.40 s, 0.80 s (top left to right) and at 1.60 s, 3.20 s and 6.40 s (bottom left to right) are based on the 10 μm apparent temperature maps. Whereas the Boeing KC-135 aircraft lap splices are held together with rivets, they have no adhesive bonds. The Boeing KC-135 Panel 2 (2FR, at the right edge) lap splice sites have significant material loss (35%-45%) from corrosion at center right of the images in Figure 6. These sites have above-ambient (1.5-1.9 ^{o}C) temperature rises which remain constant from 0.4 s to 0.8 s, unlike the above-ambient (0.2-0.6 ^{o}C) Boeing 737 (s26f400.7) corroded lap splice sites which remain constant from 0.4 s to 3.2 s.

At late times >0.4 s, temperature versus time responses differ for lap splice sites on the Boeing 737 (with adhesive bonds at sites not destroyed by corrosive activity) and the Boeing KC-135 (without adhesive bonds). At early time <0.4 s, this is less evident. Our analyses of DBIR images (at 0.4 s after the heat flash) depicted corrosive activity at a site where visual indicators of corrosion were apparent for the Boeing 737 aircraft lap splice (e.g., pillowing around rivet heads) at Stringer 26, Station F400.7. This lap splice was on the belly of the aircraft, beneath the galley and the latrine, a likely spot for corrosion to occur.

7.0 CORRELATION OF THICKNESS LOSS WITH SURFACE TEMPERATURE RISE

We established the correlation between percent thickness loss and degree Celsius surface temperature rise, at 0.4 seconds after the heat flash, based on measurements for the following five specimens which averaged 24 ± 5 % thickness loss per ^{o}C.

- F-18 corroded wing box structure from Northrop Corporation (2.9 mm uncorroded thickness): 22.1 ± 6.0 % per ^{o}C
- LLNL panel with milled flat-bottom holes, PanS (1.0 mm thickness): 22.7 ± 10.0 % per ^{o}C
- Bales Scientific Instruments milled flat-bottom panel from Delta Airlines, B1 (1.1 mm thickness): 25.8 ± 4.5 % per ^{o}C
- Bales Scientific Instruments milled flat-bottom panel from Delta Airlines, B2 (2.3 mm thickness): 31.5 ± 4.8 % per ^{o}C
- LLNL aluminum plate, B3 (1.5 mm), combined with B2 to form B2B3 (3.9 mm thickness): 17.2 ± 1.8 % per ^{o}C.

The correlation of thickness loss with surface temperature rise provides an important step in quantifying the amount of corrosion in aircraft lap splices. See Table 1. However, what may appear to be the surface temperature "finger prints" of corrosion for some cases, may not be for other cases. Thermal "finger prints" may be able to quantify material loss effects from corrosion for one or two loose, flat, overlapping panels, but not necessarily for a tightly riveted lap splice with production ripples backed by doublers and stringers. Trapped air within rippled, multiple structures (consisting of three or more separate panels) may produce surface temperature rises which mask the true, quantitative thickness loss effects from corrosion in a flat, riveted lap splice. Further work is expected to determine unique, time-dependent thermal signatures which distinguish corrosion-related thickness losses from other effects.

Table 1. Measured 10 μm IR temperature differences for several calibration panels which had on the average 24 ± 5 % material loss per 1 °C above ambient surface temperature rise at 0.4 s after the heat flash (left side). This correlation between material loss and above ambient surface temperature rise was used to determine the percentage material loss from corrosion for the Stringer 26 Boeing 737 lap splice panels (center) and the Boeing KC-135 aircraft lap splice inspection panels (right side).

Panel	Spot	T	ΔT	%Loss	Panel	Spot	T	ΔT	%Loss	Panel	Spot	T	ΔT	%Loss
B1	0	30.8	0.3	7 (2)	s26	0	25.8	0.6	14	2FL	0	27.2	0.0	0
%Loss	1	30.7	0.2	n.a.	f420.5	1	25.6	0.4	9		1	27.6	0.4	9
0=9%	2	31.3	0.8	19 (4)	max %	2	25.4	0.2	5	max %	2	27.4	0.2	5
2=19%	3	30.5	0.0	0	(Std D)	3	25.5	0.3	7	(Std D)	3	27.4	0.2	5
4=28%	4	31.7	1.2	29 (6)	14	4	25.5	0.3	7	9	4	27.6	0.4	9
	5	30.5	0.0	0	(4)	5	25.3	0.1	2	(3)	5	27.4	0.2	5
1.1mm	6	30.7	0.2	n.a.		6	25.4	0.2	5		6	27.6	0.4	9
	7	30.3	-0.2	n.a.		7	25.3	0.1	2		7	27.4	0.2	5
PanS	0	34.6	0.6	14 (6)	s26	0	25.4	0.3	7	2fC	0	29.2	1.8	42
%Loss	1	33.9	-0.1	n.a.	f420	1	25.4	0.3	7		1	29.3	1.9	45
0=20%	2	36.3	2.3	52(22)	max %	2	25.4	0.3	7	max %	2	28.9	1.5	35
2=40%	3	34.2	0.2	n.a.	(Std D)	3	25.2	0.1	2	(Std D)	3	28.0	0.6	14
4=62%	4	38.7	4.7	107(46	9	4	25.4	0.3	7	45	4	28.7	1.3	31
	5	34.0	0.0	0	(3)	5	25.4	0.3	7	(9)	5	28.8	1.4	33
1.0mm	6	34.0	0.0	0		6	25.4	0.3	7		6	28.4	1.0	24
	7	34.0	0.0	0		7	25.5	0.4	9		7	27.4	0.0	0
B2	0	28.2	0.3	9 (1)	s26	0	25.4	0.4	9	2FRC	0	30.1	2.2	52
%Loss	1	28.1	0.2	n.a.	f400.7	1	25.4	0.4	9		1	29.6	1.7	40
0=10%.	2	28.6	0.7	22 (3)	max %	2	25.3	0.3	7	max %	2	29.1	1.2	28
2=19%	3	28.1	0.2	n.a.	(Std D)	3	25.6	0.6	14	(Std D)	3	29.1	1.2	28
4=28%	4	28.9	1.0	32 (4)	14	4	25.4	0.4	9	52	4	29.2	1.3	31
	5	28.2	0.3	n.a.	(4)	5	25.6	0.6	14	(11)	5	29.2	1.3	31
2.3mm	6	28.1	0.2	n.a.		6	25.3	0.3	7		6	28.4	0.5	12
	7	28.1	0.2	n.a.		7	25.4	0.4	9		7	27.9	0.0	0
B2B3	0	28.9	0.3	5 (1)	s26	0	25.6	0.6	14	2FR	0	28.7	0.9	21
%Loss	1	28.6	0.0	0	f400.3.	1	25.4	0.4	9		1	28.4	0.6	14
0=6%	2	29.3	0.7	12 (2)	max %	2	25.4	0.4	9	max %	2	27.8	0.0	0
2=12%	3	28.6	0.0	0	(Std D)	3	25.1	0.1	2	(Std D)	3	28.7	0.9	21
4=17%	4	29.6	1.0	17 (3)	14	4	25.3	0.3	7	31	4	29.1	1.3	31
	5	28.4	-0.2	n.a.	(4)	5	25.4	0.4	9	(6)	5	29.0	1.2	28
3.9mm	6	28.7	0.1	n.a.		6	25.3	0.3	7		6	28.1	0.3	7
	7	28.6	0.0	0		7	25.1	0.1	2		7	28.5	0.7	17

8.0 SUMMARY AND CONCLUSIONS

We applied dual-band infrared imaging for wide area inspection of a Boeing 737 aircraft owned by the AANC, Sandia in Albuquerque, NM and several Boeing KC-135 aircraft panels used for the round robin experiment at Tinker AFB, OK. We analyzed selective DBIR image ratios which enhance surface temperature contrast and remove surface-emissivity clutter (from dirt, dents, tape, markings, ink, sealants, uneven paint, paint stripper, exposed metal and roughness variations).

We established the correlation of percent thickness loss with surface temperature rise (above ambient) for a flash-heated, partially corroded F-18 wing box structure (with a 2.9 mm uncorroded thickness) and several aluminum plates (with 1.0, 1.1, 2.3 and 3.9 mm thicknesses) which had 6 to 60 % thickness losses at milled flat-bottom hole sites. Based on this correlation, lap splice temperatures rise 1 °C per 24 ± 5 % material loss at 0.4 s after the heat flash. Corrosion by-products played a less significant role than the statistical uncertainties (which were 21 %).

We note that thickness related surface temperature differences for the flash-heated (one or two panel) laboratory test specimens, at 0.4 s after the flash, were mostly <2.4 °C. These temperature differences were comparable to the measured surface temperature differences for the flash-heated Boeing KC-135 aircraft lap splice panels. They were about four times larger than the measured surface temperature differences for the flash-heated Boeing 737 aircraft lap splice panels.

We cannot rule out the possibility that some other structural feature (apart from corrosion) might produce comparable surface temperature differences masking the effects of corrosion. Thus, some alternative method (e.g., disassembling the riveted panels, observing them visibly and applying direct thickness measurement techniques) is needed to verify whether or not we correctly interpreted corrosion as the origin of the detected surface temperature differences on the flash-heated aircraft panels.

By recording and processing the 12 bit digital images, we had the necessary flexibility to scale the image data for an extended temperature range (suitable for extensive corrosive activity) or to resolve small temperature differences for a narrow range (suitable for minimal corrosive activity). By recording thickness-loss effects related to surface temperature increases at 0.4 s after the heat flash, we avoided the late time masking effect of disbonds which delay heat transfer from the front to the back surface (e.g., for the Boeing 737 fuselage lap splice structure).

Thermal inertia maps were used effectively. They depicted bulk thermal property differences and minimized nonuniformities in the heat source. Late time thermal inertia maps (at 1.6 to 8.0 s for the Boeing 737 and 0.4 to 4.0 s for the Boeing KC-135) depicted lap splice sites with corrosion-related material losses. These lap splice sites had bulk thermal properties which provided less resistance to temperature change than their surroundings.

The Boeing 737 aircraft fuselage lap splice on Stringer 26 had corrosion-related thickness losses, between rivets (relative to the least corroded lap splice site per image) typically from as low as 2 ± 2 % to as high as 14 ± 3 %; whereas, the Boeing KC-135 Inspection Panel 2 had lap splice thickness losses ranging from 2 ± 2 % to 52 ± 11 % (see Table 1). A comparison of these results for the KC-135 with results based on other methods, once the riveted aircraft panels have been taken apart, visually inspected and subjected to other thickness measurement methods, will be the subject of a future paper.

Dynamic thermal tomography for nondestructive inspection of aging aircraft offers a promising new technique for aging aircraft inspection. This emerging technology is at the early stage of development. More work is needed to verify that the implications based on laboratory calibration standards are consistent with the effects of corrosion on actual aircraft structures.

9.0 ACKNOWLEDGMENTS

This work was performed by LLNL under the auspices of DOE contract number W-7405-ENG-48 for the FAA Aging Aircraft Non-Destructive Inspection R&D Program, Interagency Agreement DTFA03-92-A-00007. We thank Chris Seher, P. K. Bhagat and David Galella at the FAA Technical Center for their helpful suggestions. We acknowledge the support efforts of Gary Phipps, Craig Jones, Don Harmon and Pat Walter at AANC, Sandia National Laboratory, Albuquerque, NM. Also, we are grateful for the special efforts by Don Nieser and Deric Kraxberger at Tinker AFB, OK for providing the Boeing KC-135 Panels, used for the round robin experiment, to LLNL for our DBIR imaging inspections. We appreciate Maurice Bales and Chip Bishop, Bales Scientific Inc., for the loan of calibration panels obtained from Delta Airlines and for their support demonstrating the Bales DBIR Imaging System and NDI Workstation at the FAA/AANC hangar in Albuquerque and Owen Manning, Northrop Corporation, for the loan of a corroded F-18 wing box structure. We credit our colleague and research consultant, Professor Vladimir Vavilov, from the Tomsk Research Institute of Nondestructive Testing, Tomsk, Russia with the concept "dynamic thermal tomography". We acknowledge the support of Dr. Satish Kulkarni, Engineering Sciences Division, NDE Section Leader at LLNL.

10.0 REFERENCES

1. N. Del Grande, "Airborne and Field Temperature Surveys Compared At Long Valley KGRA, California", Geothermal Resources Council Transactions 5, 71 (1978).

2. N. K. Del Grande, "Airborne Temperature Survey Maps of Heat Flow Anomalies for Exploration Geology", Proceeding of International Symposium on Remote Sensing of Environment, Second Thematic Conference on Remote Sensing for Exploration Geology, Dec. 1982. Reprinted in Geothermal Resources Council Bulletin 14, p.3, Mar. 1985.

3. N. K. Del Grande, G. A. Clark, P. F. Durbin, D. J. Fields, J. E. Hernandez and R. J. Sherwood, "Buried Object Remote Detection For Law Enforcement", Surveillance Technologies, SPIE Vol. 1479, 335 (1991).

4. N. K. Del Grande, "Temperature Evaluated Mine Position Survey (TEMPS) Application of Dual Band Infrared Methodology", Proceedings of the 1990 Meeting of the IRIS Specialty Group on Passive Sensors, IRIA/ERIM sponsored symposium, March 1990.

5. N. K. Del Grande, "Sensor Fusion Methodology for Remote Detection of Buried Land Mines", Proceedings of the 3rd National Symposium on Sensor Fusion, Orlando, Fl, Vol. 1, IIAC/ERIM, p.407, August 1990.

6. Nancy Del Grande, "Airborne Detection Of Buried Minefields", Energy and Technology Review, University of California LLNL Report, UCRL-52000-91-12, (1991).

7. N. K. Del Grande, P. F. Durbin, M. R. Gorvad, D. E. Perkins, G. A. Clark, J. E. Hernandez and R. J. Sherwood, "Dual-band Infrared Capabilities for Imaging Buried Object Sites" in Proceedings of SPIE Conference 1942: Underground and Obscured Object Imaging and Detection, Ed. Nancy Del Grande, Ivan Cindrich and Peter Johnson, Orlando FL (1993).

8. G. A. Clark, J. E. Hernandez, S. K. Sengupta, R. J. Sherwood, P. C. Schaich, M. R. Buhl, R. J. Kane, M. J. Barth, N. K. Del Grande, "Sensor Feature Fusion for Detecting Buried Objects", Proceedings of SPIE Conference 1942: Underground and Obscured Object Imaging and Detection, Ed. Nancy Del Grande, Ivan Cindrich and Peter Johnson, Orlando FL (1993).

9. N. K. Del Grande, P. F. Durbin and D. E. Perkins, "Dual-Band Infrared Imaging Applications: Locating Buried Minefields, Mapping Sea Ice, And Inspecting Aging Aircraft", Review of Progress in Quantitative Nondestructive Evaluation, Ed. D. O. Thompson and D. E. Chimenti, Plenum Pr. NY, 12A, 465-472, 1993.

10. John E. Lewis, Nancy Del Grande, Ian McKendry, Philip Durbin and Matti Lepparanta, "Thermal Mapping" in ERS-1 Baltic Sea Ice Calibration/Validation Post-Experiment Report / Pipor/Finland, Finnish Institute of Marine Research Report 1992 (9), Ed. Matti Lepparanta and Mikko Lensu, Helsinki (1992).

11. P. F. Durbin, N. K. Del Grande, K. W. Dolan, D. E. Perkins and A. B. Shapiro, "Dual-Band Infrared Thermography for Quantitative Nondestructive Evaluation" Joint Army, Navy, NASA, Air Force (JANNAF) NDE Subcommittee Meeting Proceedings, Apr. 1993.

12. N. K. Del Grande, K. W. Dolan, P. F. Durbin, M. R. Gorvad, B. T. Kornblum, D. E. Perkins, D. J. Schneberk and A. B. Shapiro, "Three-Dimensional Dynamic Thermal Imaging of Structural Flaws by Dual-band Infrared Computed Tomography" in Proceedings of SPIE Conference 1942: Underground and Obscured Object Imaging and Detection, Ed. Nancy Del Grande, Ivan Cindrich and Peter Johnson, Orlando FL (1993).

13. L. A. LeSchack and N. K. Del Grande, "A Dual-Wavelength Thermal Infrared Scanner As A Potential Airborne Geophysical Exploration Tool", Geophysics 41, 1318 (1976).

14. H. S. Carslaw and J. C. Jaeger, Conduction of Heat in Solids, 2nd Edition, Oxford Univ. Pr., London, pp. 101, 112, 259, 1980.

15. Arthur B. Shapiro, "TOPAZ - A three-dimensional finite element heat transfer code, Lawrence Livermore Laboratory Report UCID-20484, August 1985.

16. V. P. Vavilov and X. Maldague, "Dynamic thermal tomography: a new promise in the IR thermography of solids", Proceedings of SPIE Conference 1682: Thermosense X1V, Ed. Jan K. Eklund, Orlando FL p. 194, 1992.

17. E. G. Grinzato, C. Bressan, P. G. Bison, A. Mazzoldi, P. Baggio, C. Bonacina, "Evaluation of moisture content in porous material by dynamic energy balance", Proceedings of SPIE Conference 1682: Thermosense X1V, Ed. Jan K. Eklund, Orlando FL p. 213, 1992.

18. Ph. M. Delpech, D. M. Boscher, F. Lepoutre, A. A. Deom and D. L. Balageas, "Quantitative nondestructive evaluation of carbon-carbon composites by pulsed infrared thermography", in Review of Progress in Quantitative Nondestructive Evaluation, 12B, Ed. by Donald O. Thompson and Dale E. Chimenti, Plenum Press, New York and London, p. 1297, 1993.

19. Jane W. Maclachlan Spicer, "Thermographic NDT", SPIE Short Course Notes, SC37, Thermosense '93, Orlando FL Section 5, p. 13, 1993.

END

DATE FILMED

3/7/94